Efficient ultra-low voltage electrolysis of CO_2 coupling with hydrazine oxidation degradation

Weifan Pan [a,d], Jun Yuan [a], Peng Wang [a], Jun Wang [a], Yong Zhao [c], Genxiang Wang [a,b,*], Hai Yu [c], Zhenhai Wen [a,**]

[a] *CAS Key Laboratory of Design and Assembly of Functional Nanostructures, and Fujian Provincial Key Laboratory of Materials and Techniques toward Hydrogen Energy, Fujian Institute of Research on the Structure of Matter, Chinese Academy of Sciences, Fuzhou, Fujian 350002, China*
[b] *School of Energy and Power Engineering, Jiangsu University, Zhenjiang 212013, China*
[c] *CSIRO Energy, 10 Murray Dwyer Circuit, Mayfield West, NSW 2304, Australia*
[d] *University of Chinese Academy of Sciences, Beijing 100049, China*

ABSTRACT

Transforming carbon dioxide (CO_2) into valuable fuels or chemicals through electrolysis represents a promising approach to reduce the carbon footprint. Conventional CO_2 electrolysis yet faces a challenge in low energy efficiency due to the energy-intensive oxygen evolution reaction (OER) occurring at the anode. In this study, we present an advanced CO_2 electrolysis system that pairs cathodic CO_2 reduction with anodic degradation of hydrazine oxidation reaction (HzOR), enabling efficient CO_2 electrolysis at an ultra-low voltage. To achieve this objective, two precious-metal-free electrocatalysts have been designed and fabricated. Specifically, a nickel single-atom catalyst anchored on porous carbon nanofibers has been developed for cathodic CO_2-to-CO conversion, while a flower-like Ni_2Fe_2N catalyst grown *in-situ* on nickel foam has been developed for anodic HzOR. We demonstrate high efficiency of CO production ($FE_{CO} > 80\%$) at 100 mA cm^{-2} with an applied voltage of only 0.45 V by simultaneously degrading hydrazine in a flow cell.

1. Introduction

Carbon dioxide (CO_2) emissions from the combustion of fossil fuels and industrial processes have resulted in detrimental environmental issues [1–5]. Electrocatalytic conversion of CO_2 powered by renewable electricity under mild conditions is a promising way to reduce CO_2 emissions and store the renewable energy into value-added carbon materials such as carbon monoxide (CO), alcohols and hydrocarbons [6–8]. During the past decade, the product selectivity and reaction rate of CO_2 electroreduction reactions (CO_2RR) has been highly improved via optimizing catalysts and electrolysis system [9–11]. The use of gas-diffusion electrodes (GDE) has led to commercially relevant current densities (>200 mA cm^{-2}) with considerable product selectivity for single-carbon and multi-carbon production [12–14]. However, the industrial application of CO_2RR is still challenging due to the low energy efficiency, poor long-term stability, and high catalyst cost [15–18].

The CO_2RR process is commonly paired with the kinetically sluggish oxygen evolution reaction (OER) [19,20]. The OER consumes ~90% of the overall energy and the produced O_2 at anode bears limited market value [21,22]. To address these issues, the electrooxidation of organic or inorganic molecules, such as alcohols[23–26], sulfides[27], biomass [28] and other organics [29,30] with lower theoretical oxidation potentials, were employed as substitutes for the OER in CO_2 electrolysis. In comparison to these molecules, the hydrazine oxidation reaction (HzOR) exhibits a significantly lower oxidation potential of only −0.33 V *versus* reversible hydrogen (*vs*. RHE) ($N_2H_4 + 4OH^- - 4e^- \rightarrow N_2 + 4H_2O$). Notably, hydrazine hydrate is a crucial rocket fuel known for its high calorific value, stable hydration form, and environmentally friendly oxidation products. However, the treatment of waste hydrazine, largely originating from industrial and rocket waste fuels, poses a significant concern due to its high toxicity to aquatic organisms [31–35]. The coupling of CO_2 electrolysis with the electrooxidation of waste hydrazine presents an opportunity to simultaneously reduce electrical energy consumption and treat pollutants, achieving the goal of 'converting waste into treasure' at both the cathode and anode. However, this integration of CO_2RR with HzOR has seldom been implemented in a

complete electrolyzer system.

In this work, we present an energy-efficient CO_2 electrolysis system achieved by coupling the electrooxidation of waste hydrazine at the anode, resulting in a significantly reduced full-cell voltage. We have developed single atomic nickel anchored on porous carbon nanofiber (NiSACs-PCNF) as the CO_2RR catalyst and a flower-like Ni_2Fe_2N *in-situ* grown on nickel foam (Ni_2Fe_2N/NF) as the HzOR catalyst. The NiSACs catalyst demonstrates efficient CO production toward CO_2RR electrocatalysis with a CO Faradaic efficiency (FE_{CO}) of over 90% in wide potential window ranging from -0.7 to -1.2 V *vs*. RHE in 3 M KCl solution (pH = 5.5), while the Ni_2Fe_2N catalyst delivers a current density of 100 mA cm^{-2} at 0.2 V *vs*. RHE. Coupling these two reactions in a flow-scheme electrolyzer, we achieve efficient CO production (FE_{CO}>80%) at 0.45 V with current density reaching up to nearly 100 mA cm^{-2}, leading to a high full-cell energy efficiency of over 40%. This work provides insights in designing catalysts and systems for improved energy efficiency and thus accelerate the practical application of CO_2 electrolysis technology.

2. Experimental section

2.1. Materials

All reagents were commercially purchased and used as received. Raw materials involved in this work include Nickel (II) nitrate hexahydrate (AR, 98.0%), Iron (II) sulfate heptahydrate (AR, 99.0%), Melamine (AR, 99.5%), Ethanol absolute (AR, 99.7%), Potassium hydrogen carbonate (AR, 99.5%), Potassium hydroxide (AR, 85%), Potassium chloride (AR, 99.5%), Urea (AR, 99.0%), Ammonium fluoride (AR, 96.0%), Acetone (AR, 99.5%), Hydrochloric acid (AR, 36%-38%), which were purchased from Sinopharm. Poly (vinyl alcohol) 1799 (98%~99% mol/mol) and Polytetrafluoroethylene preparation (60% wt%) was purchased from Macklin. And carbon paper was obtained from HESEN (HCP120), respectively.

2.2. Synthesis of cathode electrocatalysts (NiSACs-PCNF)

Preparation of the electrospinning solution: Firstly, 0.1 mmol Ni (NO_3)·6 H_2O was dissolved in 7 mL DI water, then 900 mg polyvinyl alcohol (PVA) was added into the above solution and heated at 90 °C for 2 hours until completely dissolved. After that, 3 mL Polytetrafluoroethylene preparation (PTFE) was poured into the solution and stirred at room temperature for about 5 min to obtain the electrospinning solution.

Synthesis of the precursor fiber membrane through electrospinning: At room temperature, the electrospinning solution prepared above was injected into a 10 mL syringe with a φ1.8 mm*50 mm stainless steel needle at the tip, which is connected to the high voltage power device. The solution advancing speed was set as 0.01 mL/min, the positive voltage was set as +20.0 kV and the negative voltage as -2.0 kV. At the same time, keep the distance of needle tip and roller collector at 20 cm. Finally, peel the precursor fiber membrane off from the roller collector.

Synthesis of the final NiSACs-PCNF catalyst: The prepared precursor fiber membrane was pre-oxidized in air at 250 °C for 5 h. After that, the pre-oxidized fiber membrane was placed in a porcelain boat, and another porcelain boat loaded with melamine was placed at upstream of the carrier gas, while the mass ratio of the fiber membrane to melamine was 1:20. The specific heating procedure was as follows: in the argon atmosphere, the material was raised to 350 °C at 3 °C/min and kept for 2 h, then it was raised to 900 °C at 3 °C/min and kept for 2 h. After cooling to room temperature, NiSACs-PCNF was thus obtained. The controlled sample PCNF was prepared with the same process of preparing NiSACs-PCNF except no addition of nickel source.

2.3. Synthesis of anode electrocatalyst (Ni_2Fe_2N/NF)

Firstly, the nickel foam was cut into the size of 1.0 cm * 2.0 cm, then soaked in 2 M HCl solution and ultrasonic for 2 h to remove the nickel oxide on the surface. The clean nickel foam was obtained after being washed with acetone, ultra-pure water and ethanol for more than 3 times in sequence. Then the Ni_2Fe_2N/NF supported Ni foam was prepared via the following steps: (a) Synthesis of $Ni_2Fe_2(CO_3)(OH)_8·2\ H_2O$/NF precursor. In a typical procedure, 0.291 g Ni(NO_3)$_2$·6 H_2O and 0.278 g $FeSO_4$·7 H_2O were dissolved in 30 mL DI water. 0.185 g NH_4F and 0.601 g urea were then added in sequence to the solution under vigorous stirring at room temperature. Then the clear solution was transferred to a Teflon-lined autoclave and dipped a piece of nickel foam (1.5 cm^2) into it. After a 8-hour reaction at 120 °C, the autoclave was allowed to cool down to room temperature, the catalyst supported NF was washed by DI water and then dried in a lyophilizer for 12 h to obtain $Ni_2Fe_2(CO_3)(OH)_8·2\ H_2O$/NF, the product sediment was also washed and dried to get the $Ni_2Fe_2(CO_3)(OH)_8·2\ H_2O$ powder and used for characterization. (b) Synthesis of Ni_2Fe_2N/NF. The nitriding process of the above prepared $Ni_2Fe_2(CO_3)(OH)_8·2\ H_2O$/NF precursor was carried out under a flowing ammonia atmosphere at 550 °C for 2 h (heating rate: 3 °C/min). The obtained precursor powder also underwent the same nitrization step to get the target Ni_2Fe_2N powder catalyst, which could be used for XRD, XPS, TEM characterization.

2.4. Material characterization

Electrochemical measurements were performed on a CHI 760E electrochemical workstation (Shanghai Chenhua) in typical H-Cell (Tianjin GaossUnion) and Flow-Cell (Home-made) separated by Nafion*117 (Dupond) membrane between cathode and anode chambers. Gas phase products were analyzed by Gas Chromatography (SHIMADZU GC2014). Liquid phase products were analyzed by nuclear magnetic resonance spectrometer (1 H NMR) on ECZ600R. X-ray diffraction spectra were taken by a Rigaku Miniflex600 powder diffractometer using Cu Kα radiation (k= 1.5406 Å). X-ray photoelectron spectra analysis (XPS) was carried out using ESCALAB 250Xi (ThermoFisher). The metal content was measured by Inductive Coupled Plasma Emission Spectrometer (Ultima 2). N_2 adsorption-desorptipn was conducted at 77.35 K using a Micromeritics ASAP2460 instrument with degassing samples under vacuum at 393 K for 8 h. Field emission scanning electron microscope (FE-SEM) pictures were taken with HITACHI SU-8010.Transmission electron microscopy (TEM) images and element mapping analysis (EDS) were obtained using FEI Talos-F200S. The high-angle annular dark-field scanning transmission electron microscopy (HAADF-STEM) analysis was carried out on a EM-ARM300F TEM/STEM equipped with a spherical aberration corrector. Raman spectra were performed on a Renishaw InVia Raman Microscope with a 532 nm laser excitation. X-ray Absorption Spectroscopy (XAS, Ni K-edge) data were collected at the beamline 1W1B of the Beijing Synchrotron Radiation Facility (BSRF) in the fluorescence mode using a Lytle detector.

3. Results and discussion

3.1. Synthesis and characterizations of NiSACs-PCNF cathode catalyst

Carbon-based single-atom catalysts (SACs), capable of catalyzing the highly selective and active conversion of CO_2 into CO, stand out as prime candidates for the CO_2 reduction reaction (CO_2RR).[12,36,37] This is attributed to their distinctive merits, including corrosion resistance, maximum atom efficiency, and excellent stability. Among these reported SACs, the NiSACs achored on carbon-based nano materials commonly presented excellent CO_2RR performance with high activity, nearly unity selectivity to CO production, and robust stability over hundreds of hours without degradation [22,29,31]. Though plenty of techniques have been

used to prepare carbon-based NiSACs, there remains much space to explore controllable, stable, facile and easily scalable techniques for fabricating cost-effective carbon-based NiSACs for CO_2RR. In this work, the mass-produced electrospinning technique combined with pyrolysis was applied to prepare the cathode catalyst for CO_2RR. The nickel single atoms loaded porous-structured carbon nanofiber (NiSACs-PCNF) catalyst was fabricated *via* an electrospinning process followed by carbonization and nitridation treatments (Figs. 1a and S1). Specifically, the primary fiber was electrospun from a mixture solution consisting of polyvinyl alcohol (PVA), nickel nitrate and polytetrafluoroethylene (PTFE) suspension and deionized water. After that, the prepared fiber

membrane underwent high-temperature carbonization and nitridation through the decomposition of melamine, and the NiSACs-PCNF was finally obtained for use (more synthesis details in supporting information). The porous carbon nanofiber without Ni precursor was also prepared for comparison purpose.

The structure of the obtained nanofiber was firstly examined by scanning electron microscopy (SEM) and transmission electron microscopy (TEM), both of which confirmed the three-dimensional interconnected and porous architecture of NiSACs-PCNF that has a specific surface area of 558 m^2g^{-1} (Figs. 1b-d, S2 and S3). This unique porous structure of NiSACs-PCNF with abundant micropores (ca. 1 nm) and
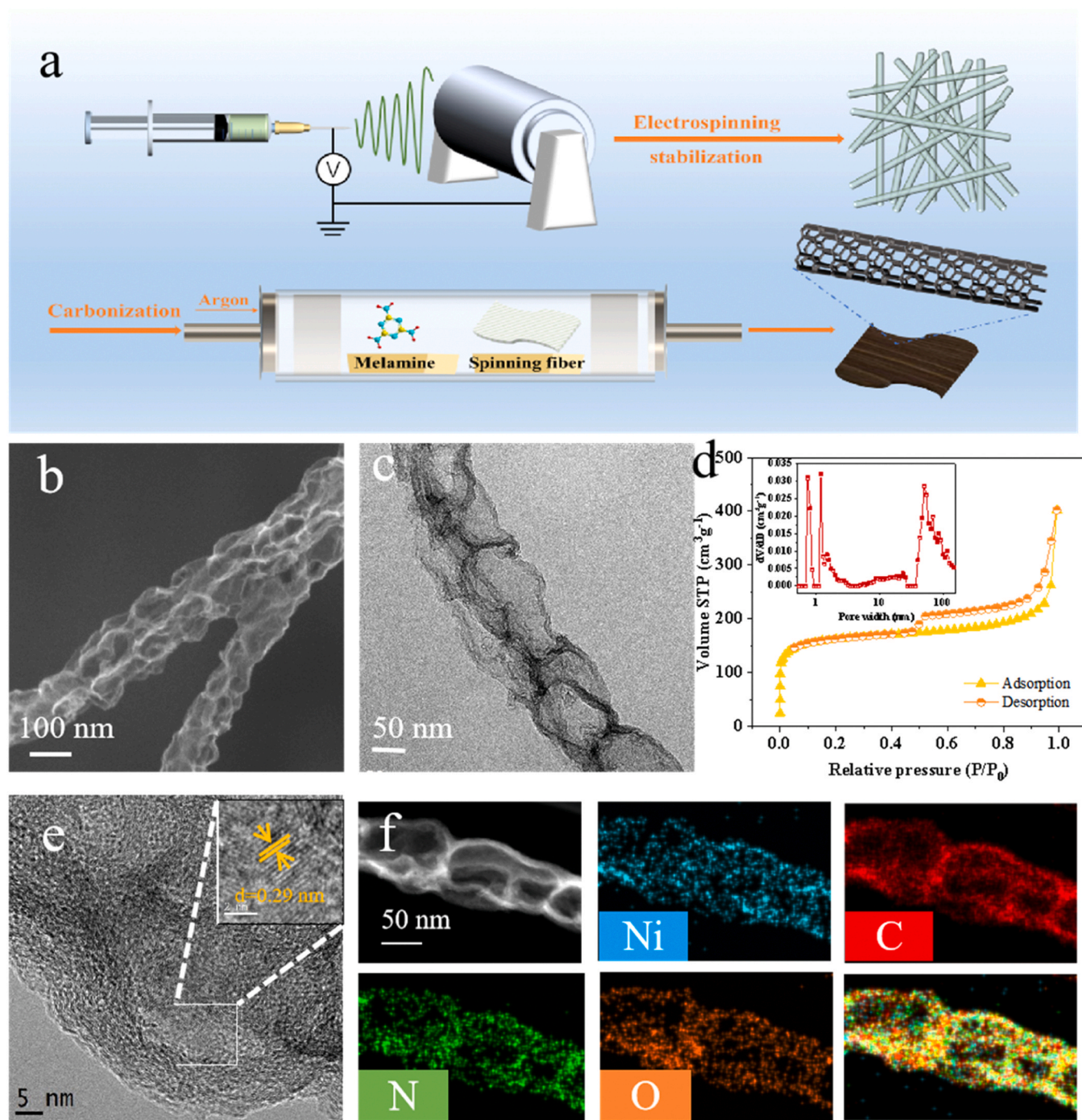

Fig. 1. Schematic illustration of the synthetic process of NiSACs-PCNF and the Structural characterizations. (a) Electrospinning of mixture solution into Ni-PVA precursor, followed by carbonization to form the NiSACs-PCNF catalyst. (b) SEM image. (c) TEM image. (d) N_2 sorption isotherms of NiSACs-PCNF, inset: Pore size distribution. (e) HRTEM image and the enlarged image. (f) EDS mappings of Ni, C, N and O elements.

macropores (ca. 50–100 nm) will not only facilitate the transfer of electrons and enhances electrical conductivity, but also enrich CO_2 around active sites. Moreover, the high-resolution TEM (HRTEM) image shows no clusters or nanoparticles in NiSACs-PCNF apart from the lattice stripes of carbon (002) crystal faces. The energy-dispersive X-ray spectroscopy elemental mapping (EDS) reveals the Ni, C, N, O elements are homogenously distributed within the structure of NiSACs-PCNF (Figs. 1e, f and S4), which coincides well with its corresponding X-ray diffraction (XRD) pattern that there are no characteristic peaks assigned to Ni or Ni oxides crystals except two diffraction peaks at 22° and 44° for carbon (Fig. 2a). The fine atomic-scale structure of Ni in NiSACs-PCNF was then studied by aberration-corrected high-angle annular dark-field scanning transmission electron microscopy (HAADF-STEM) (Fig. S5). As presented in Fig. 2b and c, the monodispersed Ni single atoms circled in red are clearly seen due to the different contrasts of Ni, N, C and O elements. Moreover, the L_2 and L_3 signals of Ni were also detected through the electron energy loss spectroscopy (EELS) analysis of the less luminous atoms on the NiSACs-PCNF catalyst, which further confirms the presence of Ni atoms. On the account of the above results, Ni sites in NiSACs-PCNF are confirmed in the form of atomic dispersion on the nanoporous fiber with Ni amount of 1.98% tested by inductively coupled plasma optical emission spectroscopy (ICP-OES, Table S1). Notably, the PCNF controlled sample without Ni single sites presents similar morphology and porous structure to that of NiSACs-PCNF (Figs. S6-S8).

The composition and element states on the surface of the prepared NiSACs-PCNF and PCNF were then detected by X-ray photoelectron spectroscopy (XPS). The N 1 s spectrum of NiSACs-PCNF can be deconvoluted into pyridinic (~398.5 eV), Ni-N (~399.6 eV), pyrrolic (~401.0 eV), quaternary (~402.6 eV) and oxidized (~404.3 eV) N species (Figs. 2d and S9), proving the existence of coordination between nickel and nitrogen atoms in NiSACs-PCNF.[38,39] For the Ni2p spectrum, the binding energy of 854.8 eV for $Ni2p_{3/2}$ locates between metallic Ni^0 (854.1 eV) peak and Ni^{2+} (855.8 eV) peak, suggesting that the oxidation state of the Ni atoms in NiSACs-PCNF likely lies between 0 and +2 [22,40,41] (Figs. S9 and S10). In Fig. 2e, Raman spectroscopy confirms the ratio of the defects and graphitization (I_D/I_G) with a D peak at 1351 cm^{-1} and a G peak at 1580 cm^{-1}, respectively. The higher I_D/I_G value (1.06) of NiSACs-PCNF indicates that NiSACs-PCNF has relatively abundant defects, thus affecting the catalytic activity of the catalyst. In addition, the X-ray absorption near-edge structure (XANES) and extended X-ray absorption fine-structure (EXAFS) spectra were further used to ascertain the formation of Ni atomic sites in NiSACs-PCNF and precisely decipher their local coordination configuration on the atomic scale (Fig. 2f). The Fourier transforms (FTs) of the EXAFS spectra of Ni K-edge (Fig. 2g) displays a predominant peak at 1.44 Å attributed to the
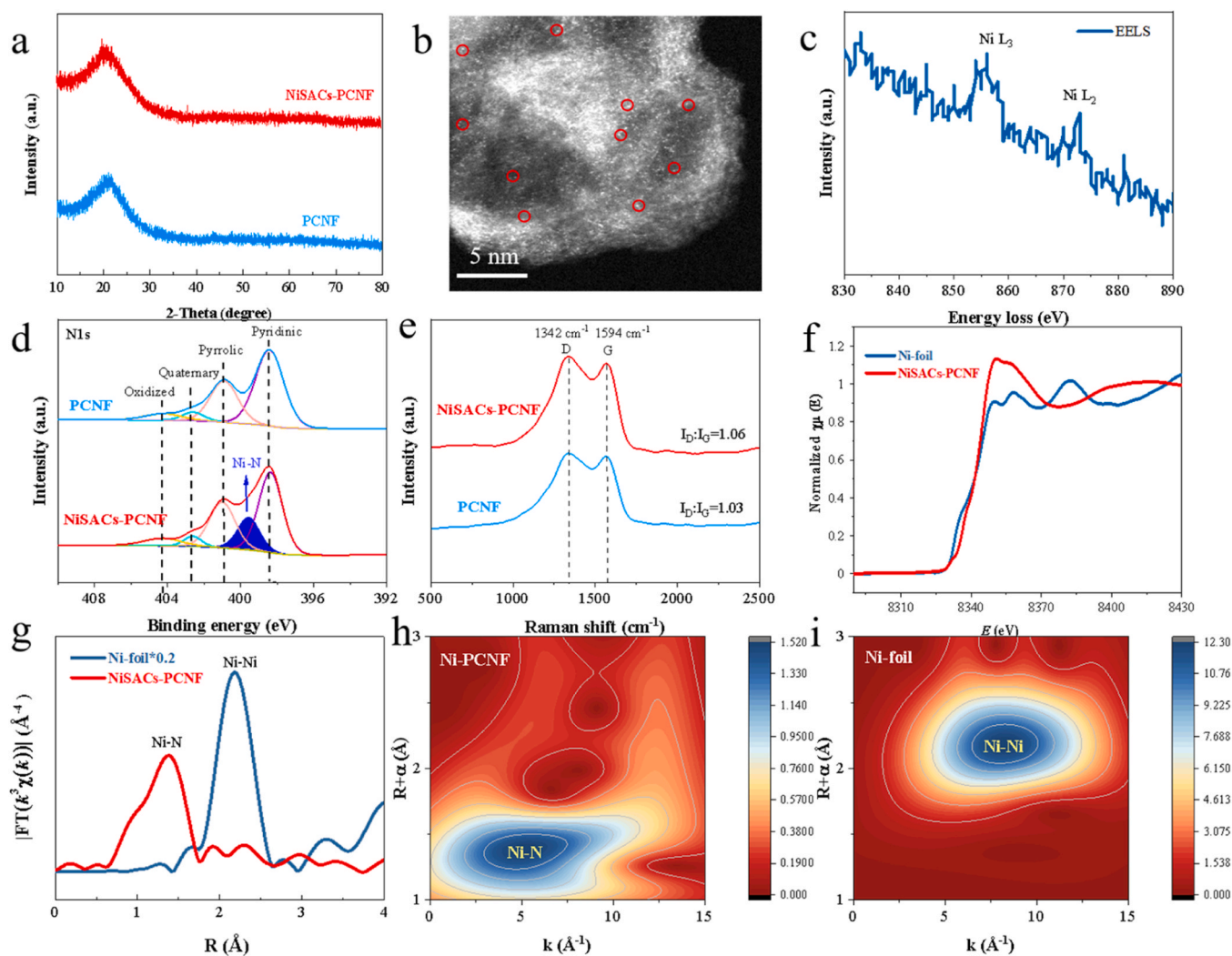

Fig. 2. Chemical analysis of NiSACs-PCNF and PCNF. (a) XRD patterns of two samples: NiSACs-PCNF and PCNF. (b) HAADF-STEM image of NiSACs. (c) EELS. (d) N1 s XPS depth profile spectrum comparison. (e) Raman spectrums of NiSACs-PCNF and PCNF samples. (f) XANES spetra of Ni-edge. (g) FTs of k^3-weighted Ni K-edge EXAFS data. (h-i) WTs for k^3-weighted Ni K-edge EXAFS signal.

Ni-N first shell coordination, and there is no metallic Ni-Ni bond in NiSACs-PCNF. Furthermore, the EXAFS wavelet transform (WT) maps with increased resolution in k-space were used to identify the overlapped contribution [42,43]. As illustrated in the WT contour plots of Ni foil, the intensity maximum at 8.2 Å^{-1} can be assigned to the Ni-Ni contribution, whereas NiSACs-PCNF shows no Ni-Ni contribution but a broad intensity maximum (5.5 Å^{-1}) at a higher R-space magnitude due to the overlap of Ni-N contributions, verifying no metal-derived crystalline structure in NiSACs-PCNF (Fig. 2h and i) [44].

3.2. CO2RR performance evaluation of NiSACs-PCNF catalyst

The electrocatalytic performance of NiSACs-PCNF catalyst and the controlled PCNF was firstly investigated in a traditional three-electrode H-Cell with a CO_2-saturated 0.5 M $KHCO_3$ solution (Figs. S11-S12),

which verifies the key role of Ni single atoms in catalyzing CO_2 reduction. In view of the issues of mass transport limitation of CO_2 in H-cell and quick carbonatation in neutral electrolyte, a home-made three-electrode flow cell system with gas diffusion electrodes was used to study the electrocatalytic performance of NiSACs-PCNF for CO_2RR with the mildly acidic electrolyte of 3 M KCl solution (pH = 5.5) as catholyte and 1 M KOH solution as anolyte (Fig. 3a). Remarkably, the current density in the flow cell reached an industrially relevant level (> 100 mA cm^{-2}) and was much larger than that in the H-Cell. This proves the superiority of the flow cell configuration. Fig. 3b shows that the NiSACs-PCNF exhibits a current density of 275 mA cm^{-2} at -1.2 V *vs.* RHE, which is 1.3 times larger than that of PCNF (200 mA cm^{-2}). The main gaseous products were determined to be CO and H_2, and no liquid products were detected for the as-prepared catalysts (Fig. S13). Fig. 3c compares the FE$_{CO}$ in the potential range of from -0.7 to -1.2 V *vs.*
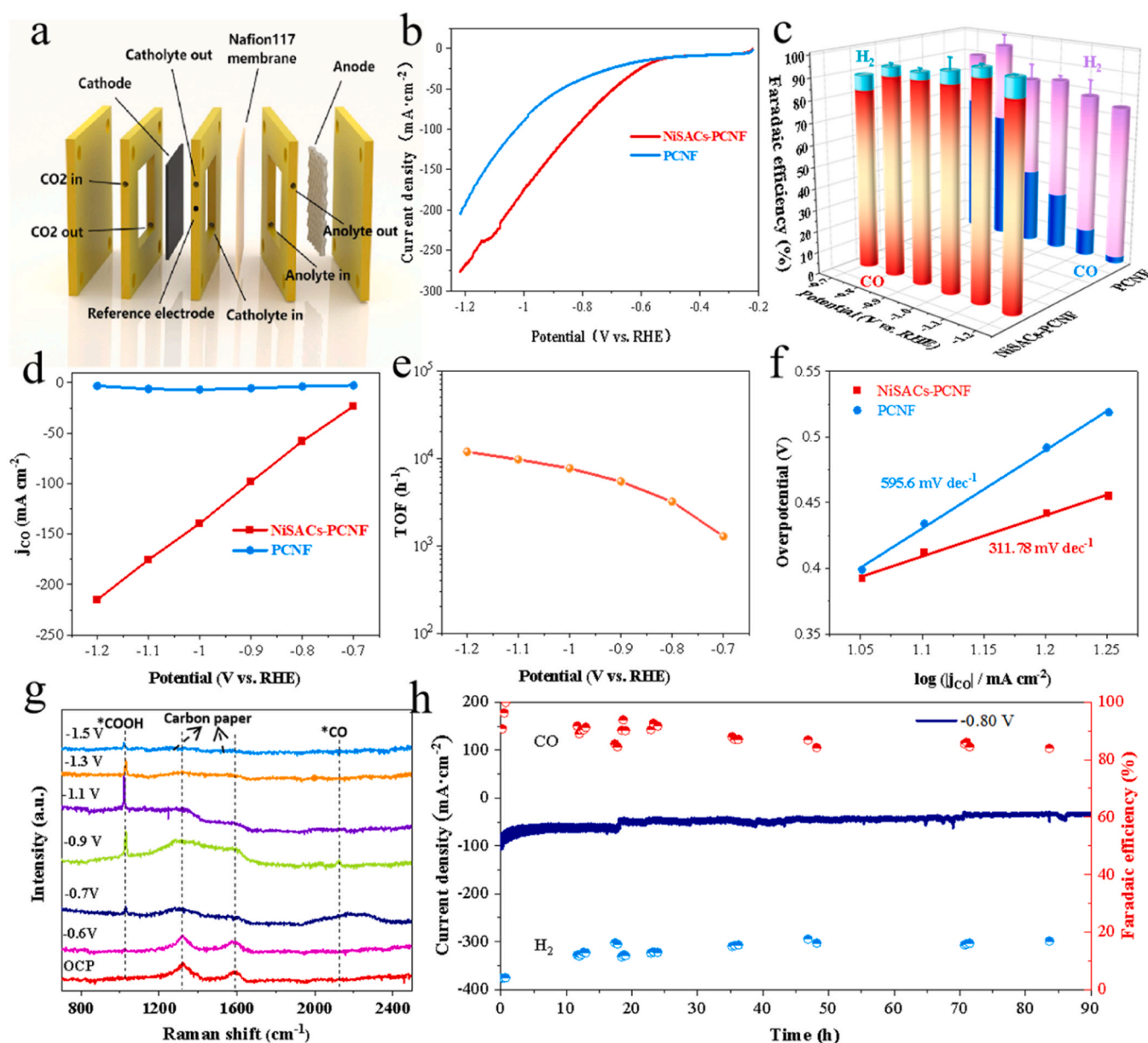

Fig. 3. Electrocatalytic activity tests in a GDE-based flow cell. (a) Schematic diagram of flow cell. (b) LSV curves of NiSACs-PCNF and PCNF in the potential range from -0.2 V to -1.2 V (catholyte: 3 M KCl solution, scan rate: 5 mV s^{-1}). (c) FE$_{CO}$ and FE$_{H2}$ at various applied potentials. (d) CO partial current densities. (e) TOF of NiSACs-PCNF at different potentials. (f) Corresponding Tafel plots of the LSV curves for NiSACs-PCNF and PCNF. (g) The *in situ* Raman spectra under different potentials over NiSACs-PCNF. (h) Time-dependent faradaic efficiency and current density of NiSACs-PCNF for CO_2RR during chronoamperometric electrolysis at -0.8 V.

RHE. Evidently, the NiSACs-PCNF demonstrates superior FE_{CO} over the entire potential range, with a maximum FE_{CO} of 98% at −1.0 V (Fig. 3c). By contrast, the FE_{CO} of the controlled PCNF is drastically lower than that of NiSACs-PCNF in the whole potential window. The CO partial current densities (j_{CO}) on these two catalysts were also plotted against the applied potential. As shown in Fig. 3d, the NiSACs-PCNF delivers much higher j_{CO} with respect to the PCNF counterpart. The j_{CO} reaches as high as 220 mA cm^{-2} on NiSACs-PCNF at −1.2 V *vs.* RHE, whereas it is only 5 mA cm^{-2} on PCNF at the same potential. The superior intrinsic activity of NiSACs-PCNF is further highlighted by calculating the turn-over frequency (TOF) in Fig. 3e. The developed NiSACs-PCNF exhibits an exceptionally high TOF of 10000 h^{-1} at −1.2 V *vs.* RHE, out-performing most of the reported SACs materials as shown in Table S2 [45]. The accelerated CO_2-CO conversion kinetics on NiSACs-PCNF is further confirmed by its lower Tafel slope of 311.8 mVdec^{-1} than that of PCNF (Fig. 3f), which reveals that the first electron transfer is the rate determination step (RDS) for CO_2RR and the Ni single atoms can effectively promote the *COOH formation and thus the overall CO_2RR

kinetics. The catalytic mechanism was further elucidated through *in-situ* Raman measurements, enabling the monitoring of intermediate profiles during CO_2 reduction process. As depicted in Fig. 3g, the peaks at around 1030 cm^{-1} can be assigned to the OCO antisymmetric streching of *COOH [46,47]. The intensity of the *COOH signal peak increases with rising potential, reaching its peak at −1.1 V *vs.* RHE, and subsequently decreases with further potential increases. In addition, despite extensive CO production, no discernible peak corresponding to *CO adsorption on the prepared catalyst was detected, indicating efficient desorption of produced CO from the reaction interface [47–49]. The above information implies that the formation of the *COOH intermediate governs the rate-determining step in the conversion CO_2 into CO process. Moreover, long-term electrolysis was performed at a stationary −0.8 V *vs.* RHE cathode potential to examine the stability of NiSCAs-PCNF, which demonstrates a superior stability without obvious degradation in current density and FE_{CO} during 90 h constant electrolysis (Fig. 3h).
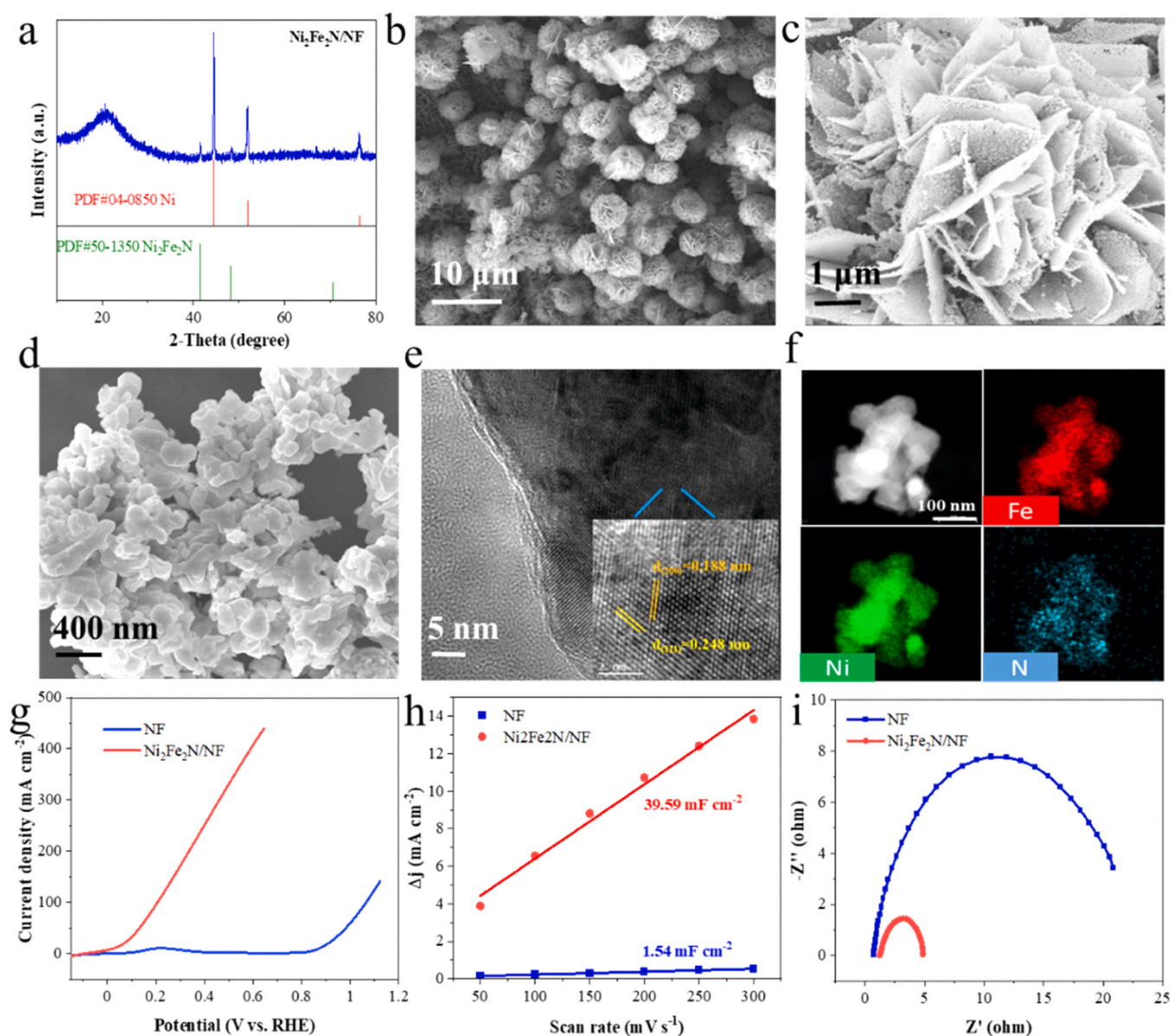

Fig. 4. Chemical characterizations of anode catalyst. (a) XRD patterns, (b-d) SEM images, (e) TEM images of Ni_2Fe_2N powder, scale bar: 5 nm and 2 nm, respectivley. (f) corresponding EDS mapping of Ni, Fe and N elements. (g) LSV curves of electrocatalysts toward HzOR. (h) Tafel plots of corresponding LSV curves. (i) EIS Nyquist plots.

3.3. Synthesis and structural characterizations of Ni_2Fe_2N/NF anode catalyst

Recent developments demonstrate the application of hydrazine as a promising fuel with distinguished advantages including low superior theoretical cell voltage, environmentally friendly products (only nitrogen and water). Noble metals have been reported with promising catalytic activity and stability for the HzOR, however, the high cost of such catalysts limits their wide uses [50,51]. In the proposed electrolyzer coupling HzOR with CO_2RR, a non-noble anode catalyzing the hydrazine oxidation reaction was designed to pair with CO_2RR in cathode. Specifically, the nanostructured Ni_2Fe_2N *in-situ* grown on Ni foam (Ni_2Fe_2N/NF) was fabricated for HzOR *via* a facile two-step method. First, we obtained the nanostructured bimetallic hydroxide carbonate precursor on Ni foam substrate through solvothermal method. Then, the resulting precursor was calcined under a NH_3 atmosphere to get the target nitride catalyst. The XRD pattern verifies the single Ni_2Fe_2N phase (PDF#50–1350) is successfully grown on NF (Figs. 4a and S14). As the SEM pictures shown in Fig. 4b-c, they depict that the catalyst owns a nanoflower structure composed of nanoflacks. The amplified SEM image in Fig. 4d shows these nanoflacks consist of a large number of cross-linked nanoparticles, which is further confirmed by the TEM image (Fig. 4e and S15). The visible lattice spacing of 0.188 nm and 0.248 nm observed in HR-TEM image can be assigned to the (200) and (111) lattice planes of Ni_2Fe_2N. In addition, its HAADF-STEM in combination with EDS elemental mapping analysis (Fig. 4f) confirms uniform distribution of Ni, Fe and N throughout the Ni_2Fe_2N nanoparticles. Furthermore, XPS analysis of the Ni_2Fe_2N powder sample was employed to confirm the surface element states (Fig. S16). Specifically, for the N 1 s, the peaks at 397.1, 400.1 and 402.5 eV can be assigned to the N-M (M: Ni, Fe), N-H and nitrided satellites. The Ni 2p spectra can be fitted into three pairs of corresponding to Ni-N, Ni-O and satellites, respectively. And the Fe 2p spectra can also be fitted into Fe-N, Fe-O and satellites [52]. The above results clearly prove the unique structural morphology and composition of the prepared catalyst.

3.4. HzOR Electrochemical performance over Ni_2Fe_2N/NF

The electrocatalytic properties of Ni_2Fe_2N/NF toward HzOR were examined in an alkaline hydrazine solution (1.0 M KOH + 0.5 M N_2H_4). As the LSV curves shown in Fig. 4g, the Ni_2Fe_2N/NF only requires a potential of 0.2 V *vs.* RHE to attain a current density of 100 mA cm^{-2} without IR compensation for HzOR, which is nearly 0.9 V lower than that (1.1 V *vs.* RHE) of NF, suggesting significantly improved catalytic activity with loading Ni_2Fe_2N. The electrochemical active surface area (ECSA) of the prepared catalyst is evaluated by the electrochemical double-layer capacitance (C_{dl}) that is proportional to ECSA (Fig. S17). Fig. 4h clearly manifests that the Ni_2Fe_2N/NF possess far larger C_{dl}, implying they are more active sites for HzOR. Moreover, the Nyquist plots of Ni_2Fe_2N/NF in the Electrochemical impedance spectroscopy (EIS) measurement reveals that Ni_2Fe_2N/NF possesses a smaller charge transfer resistance of (R_{ct}), indicating its better electronic conductivity (Fig. 4i). And the catalytic durability was determined by multistep chronopotentiometric curve in the range of 50–200 mA cm^{-2} (Fig. S18a). It is observed that the potential immediately rises to 0.95 V *vs.* RHE and then remains stable for the subsequent 3600 s. The long-term stability is assessed at an applied potential of 0.2 V *vs.* RHE during 10 h test. It is noted that the current density decays due to the consumption of hydrazine hydrate, after replacing the electrolyte, the current density can be restored to about 100 mA cm^{-2} (Fig. S18b). The above experimental results confirm the desired electrocatalytic behaviors of HzOR with the Ni_2Fe_2N/NF, which is comparable with those of reported in the lliteratures (Table S3).

3.5. Assembly energy-saving electrolyzer for CO_2 electrolysis

The elaborately designed NiSACs-PCNF and Ni_2Fe_2N/NF electrodes above both possess multiple merits of low cost, easy realization of large-scale production, high electrocatalytic performance and exceptional stability, enabling them to be ideal candidates for constructing a green electrolyzer by coupling CO_2 upgrading with hydrazine degradation. As a proof of concept, we assembled the energy-saving electrolyzer for CO_2 electrolysis. The cathode for CO_2RR consisted of NiSACs-PCNF supported on carbon paper (NiSACs-PCNF/CP), immersed in 3 M KCl. Simultaneously, the anode for HzOR was composed of Ni_2Fe_2N/NF, placed in 1 M KOH containing 0.5 M hydrazine solution. This configuration is denoted as NiSACs-PCNF/CP│3 M KCl (aq) ‖ 1 M KOH + 0.5 M N_2H_4 (aq)│Ni_2Fe_2N/NF. The schematic diagram briefly illustrates the assembled flow electrolyzer as shown in Figs. 5a and S19. Within the flow cell, hydrazine undergoes electrical oxidation at the alkaline anode, with electrons subsequently transferred to the cathode through the external circuit. These electrons are consumed at the cathode to reduce CO_2 into CO, while K$^+$ ions complete the circuit by traversing from the anode to the cathode chamber through the cation exchange membrane (Nafion 117 membrane in this work). In Fig. 5b, the LSV curves of the flow cell indicates that only an applied voltage of only 0.45 V is needed to achieve an electrolytic current density of 100 mA cm^{-2}, which is far lower than the voltage required for the traditional electrolyzer that pairs CO_2RR with OER in anode (2.07 V) (Fig. S20). The significant reduction in the input voltage confirms the effectiveness of the proposed electrolysis system. Furthermore, the cathodic products at different applied cell voltages were analyzed as shown in Fig. 5c and d, which presents that a maximum FE_{CO} of 80% and a full-cell energy efficiency for CO generation of ∼44% can be obtained at 0.4 V.[53] Notably, Then the long-term operation stability was assessed at 0.4 V, which demonstrated that the current density maintained nearly constant at around 40 mA cm^{-2} during 15 h of continuous electrolysis without large fluctuation in selectivity (Fig. 5e). Moreover, the pH variations of both electrolytes were monitored during long-term test in the two-electrode electrolyzer system. As illustrated in Fig. S22, the pH of the catholyte increased from 5.50 to 7.39 over the course of electrolysis, while the pH of the anolyte did not exhibit significant variations. This gradual rise in the catholyte's pH can be attributed to the consumption of H$^+$ ions in catholyte during the CO_2 reduction process.

4. Conclusion

In summary, we have proposed the concept of a promising green electrolyzer that couples cathodic CO_2RR for CO_2 valorization with anodic HzOR for hydrazine degradation, and successfully verified its feasibility through fabricating excellent catalysts in both cathode and anode. The NiSACs-PCNF as the cathodic catalyst can realize high FE_{CO} of over 90% under an industrial current density of around 100 mA cm^{-2}, while the Ni_2Fe_2N/NF as the anode for HzOR can delivery a current density of 100 mA cm^{-2} at only 0.2 V. Assembled with these two catalysts, the dual green cell (NiSACs-PCNF/CP│3 M KCl (aq) ‖ 1 M KOH + 0.5 M N_2H_4 (aq)│Ni_2Fe_2N/NF) can reach a large current density of 100 mA cm^{-2} at an ultra-low potential of 0.45 V with high CO selectivity, yielding a rather high full-cell energy efficiency of over 40% for CO production. This coupling strategy provides an innovative reference for the production of syngas through CO_2RR with low energy consumption.

CRediT authorship contribution statement

Hai Yu: Visualization, Formal analysis. **Zhenhai Wen:** Writing – review & editing, Supervision, Conceptualization. **Yong Zhao:** Formal analysis. **Genxiang Wang:** Writing – review & editing, Supervision, Investigation. **Peng Wang:** Methodology, Investigation. **Jun Wang:** Methodology. **Weifan Pan:** Writing – original draft, Methodology,
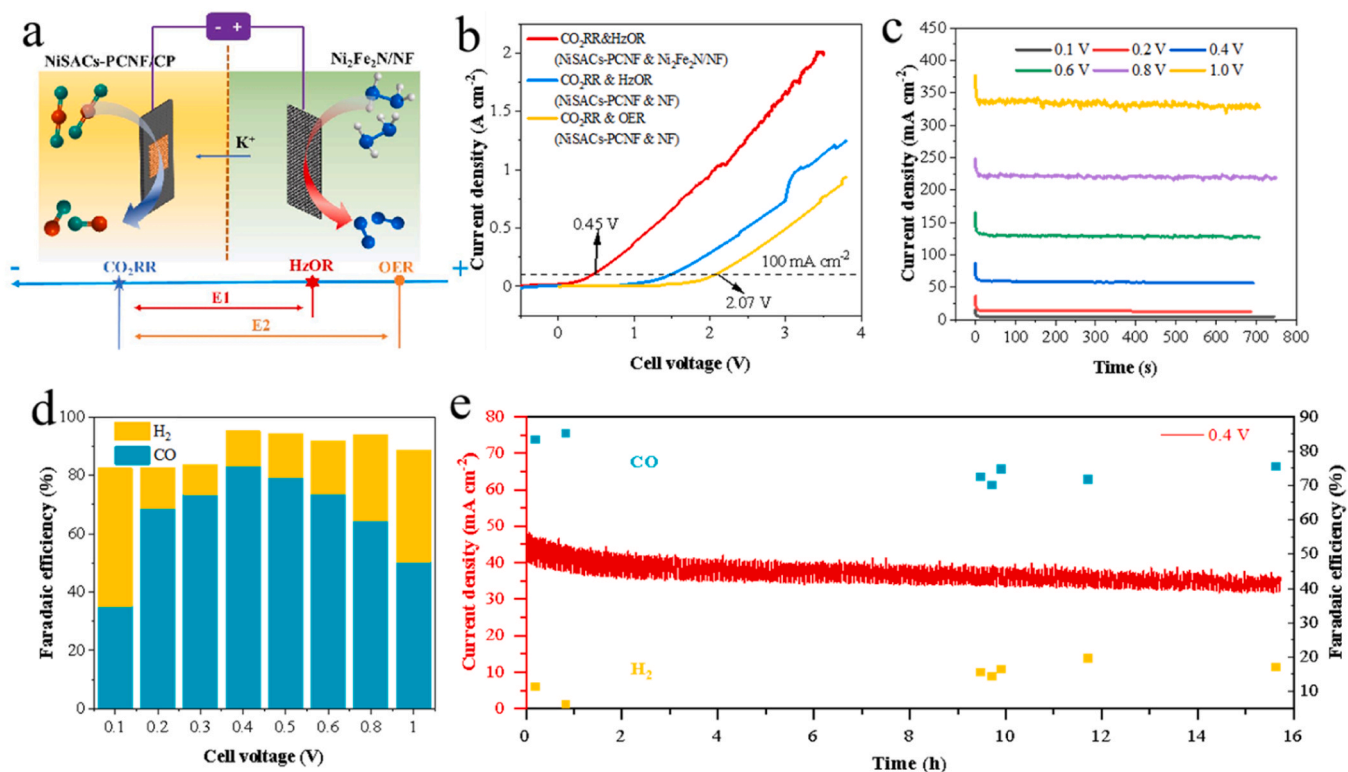
Fig. 5. Electrocatalytic investigation. (a) Diagram of flow cell Coupling CO_2RR with HzOR, Ni-PCNF as cathode and Ni_2Fe_2N/NF as anode. (b) Comparison of LSV curves while using different anolytes and anodes. (c) Current-time curves at various applied cell voltages. (d) FE_{CO} and FE_{H2} in different cell voltage. (e) Long-term stability test at 0.4 V.

Investigation, Conceptualization. **Jun Yuan:** Methodology, Investigation.

Declaration of Competing Interest

The authors declare that they have no known competing financial interests or personal relationships that could have appeared to influence the work reported in this paper.

Data availability

Data will be made available on request.

Acknowledgements

Appendix A. Supporting information

Supplementary data associated with this article can be found in the online version at doi:10.1016/j.apcatb.2024.124011.

References

[1] X. Duan, J. Xu, Z. Wei, J. Ma, S. Guo, S. Wang, H. Liu, S. Dou, Metal-free carbon materials for CO_2 electrochemical reduction, Adv. Mater. 29 (2017) 1701784.

[2] M. Li, H. Wang, W. Luo, P.C. Sherrell, J. Chen, J. Yang, Heterogeneous Single-Atom Catalysts for Electrochemical CO_2 Reduction Reaction, Adv. Mater. 32 (2020) e2001848.

[3] S. Shen, J. He, X. Peng, W. Xi, L. Zhang, D. Xi, L. Wang, X. Liu, J. Luo, Stepped surface-rich copper fiber felt as an efficient electrocatalyst for the CO_2RR to formate, J. Mater. Chem. A 6 (2018) 18960–18966.

[4] J.-J. Wang, X.-P. Li, B.-F. Cui, Z. Zhang, X.-F. Hu, J. Ding, Y.-D. Deng, X.-P. Han, W.-B. Hu, A review of non-noble metal-based electrocatalysts for CO_2 electroreduction, Rare Met. 40 (2021) 3019–3037.

[5] G. Wang, J. Chen, Y. Ding, P. Cai, L. Yi, Y. Li, C. Tu, Y. Hou, Z. Wen, L. Dai, Electrocatalysis for CO_2 conversion: from fundamentals to value-added products, Chem. Soc. Rev. 50 (2021) 4993–5061.

[6] J. Wang, S. Kattel, C.J. Hawxhurst, J.H. Lee, B.M. Tackett, K. Chang, N. Rui, C. J. Liu, J.G. Chen, Enhancing activity and reducing cost for electrochemical reduction of CO_2 by supporting palladium on metal carbides, Angew. Chem. Int. Ed. 58 (2019) 6271–6275.

[7] J. Wang, G. Wang, J. Zhang, Y. Wang, H. Wu, X. Zheng, J. Ding, X. Han, Y. Deng, W. Hu, Inversely Tuning the CO_2 Electroreduction and Hydrogen Evolution Activity on Metal Oxide via Heteroatom Doping, Angew. Chem. Int. Ed. 60 (2021) 7602–7606.

[8] Y. Chen, J. Zhang, J. Tian, J. Guo, F. Xu, Y. Zhang, X. Wang, L. Yang, Q. Wu, Z. Hu, Hierarchical Ni/N/C Single-Site Catalyst Achieving Industrial-Level Current Density and Ultra-Wide Potential Plateau of High CO Faradic Efficiency for CO_2 Electroreduction, Adv. Funct. Mater. 33 (2023) 2214658.

[9] H. Xie, T. Wang, J. Liang, Q. Li, S. Sun, Cu-based nanocatalysts for electrochemical reduction of CO2, Nano Today 21 (2018) 41–54.

[10] X. Wei, S. Wei, S. Cao, Y. Hu, S. Zhou, S. Liu, Z. Wang, X. Lu, Cu acting as Fe activity promoter in dual-atom Cu/Fe-NC catalyst in CO_2RR to C_1 products, Appl. Surf. Sci. 564 (2021) 150423.

[11] W. Pan, P. Wang, L. Fan, K. Chen, L. Yi, J. Huang, P. Cai, X. Liu, Q.-S. Chen, G. Wang, Z. Wen, Cu-Ni Alloy Decorating N-Doped Carbon Nanosheets toward High-performance Electrocatalysis of Mildly Acidic CO_2 Reduction, Inorg. Chem. Front. 10 (2023) 2276–2284.

[12] J. Zhang, W. Cai, F.X. Hu, H. Yang, B. Liu, Recent advances in single atom catalysts for the electrochemical carbon dioxide reduction reaction, Chem. Sci. 12 (2021) 6800–6819.

[13] Y. Wang, H. Su, Y. He, L. Li, S. Zhu, H. Shen, P. Xie, X. Fu, G. Zhou, C. Feng, D. Zhao, F. Xiao, X. Zhu, Y. Zeng, M. Shao, S. Chen, G. Wu, J. Zeng, C. Wang, Advanced electrocatalysts with single-metal-atom active sites, Chem. Rev. 120 (2020) 12217–12314.

[14] T. Burdyny, W.A. Smith, CO_2 reduction on gas-diffusion electrodes and why catalytic performance must be assessed at commercially-relevant conditions, Energy Environ. Sci. 12 (2019) 1442–1453.

[15] S. Ren, D. Joulié, D. Salvatore, C.P. Berlinguette, Molecular electrocatalysts can mediate fast, selective CO_2 reduction in a flow cell, Science 365 (2019) 367–369.

[16] X. Zhang, J. Li, Y.Y. Li, Y. Jung, Y. Kuang, G. Zhu, Y. Liang, H. Dai, Selective and High Current CO_2 Electro-Reduction to Multicarbon Products in Near-Neutral KCl Electrolytes, J. Am. Chem. Soc. 143 (2021) 3245–3255.

[17] X. Tan, C. Yu, Y. Ren, S. Cui, W. Li, J. Qiu, Recent advances in innovative strategies for the CO_2 electroreduction reaction, Energy Environ. Sci. 14 (2021) 765–780.

[18] E.W. Lees, B.A.W. Mowbray, D.A. Salvatore, G.L. Simpson, D.J. Dvorak, S. Ren, J. Chau, K.L. Milton, C.P. Berlinguette, Linking gas diffusion electrode composition to CO_2 reduction in a flow cell, J. Mater. Chem. A 8 (2020) 19493–19501.

[19] A. Peugeot, C.E. Creissen, M.W. Schreiber, M. Fontecave, Advancing the Anode Compartment for Energy Efficient CO_2 Reduction at Neutral pH, ChemElectroChem 8 (2021) 2726–2736.

[20] M. Li, T. Wang, W. Zhao, S. Wang, Y. Zou, A Pair-Electrosynthesis for Formate at Ultra-Low Voltage Via Coupling of CO_2 Reduction and Formaldehyde Oxidation, Nano-Micro Lett. 14 (2022) 211.

[21] Z. Xu, C. Peng, G. Zheng, Coupling Value-Added Anodic Reactions with Electrocatalytic CO_2 Reduction, Chem. Eur. J. 29 (2022) e202203147.

[22] G. Wang, J. Chen, K. Li, J. Huang, Y. Huang, Y. Liu, X. Hu, B. Zhao, L. Yi, T. W. Jones, Z. Wen, Cost-effective and durable electrocatalysts for Co-electrolysis of CO_2 conversion and glycerol upgrading, Nano Energy 92 (2022) 106751.

[23] J. Li, G. Liu, B. Liu, Z. Min, D. Qian, J. Jiang, J. Li, Fe-doped $CoSe_2$ nanoparticles encapsulated in N-doped bamboo-like carbon nanotubes as an efficient electrocatalyst for oxygen evolution reaction, Electro. Acta 265 (2018) 577–585.

[24] X. Wei, Y. Li, L. Chen, J. Shi, Formic Acid Electro-Synthesis by Concurrent Cathodic CO_2 Reduction and Anodic CH_3OH Oxidation, Angew. Chem. Int. Ed. 60 (2021) 3148–3155.

[25] S. Verma, S. Lu, P.J.A. Kenis, Co-electrolysis of CO_2 and glycerol as a pathway to carbon chemicals with improved technoeconomics due to low electricity consumption, Nat. Energy 4 (2019) 466–474.

[26] S. Guo, Y. Liu, Y. Huang, H. Wang, E. Murphy, L. Delafontaine, J. Chen, I. V. Zenyuk, P. Atanassov, Promoting Electrolysis of Carbon Monoxide toward Acetate and 1-Propanol in Flow Electrolyzer, ACS Energy Lett. 8 (2023) 935–945.

[27] X. Teng, K. Shi, L. Chen, J. Shi, Coupling Electrochemical Sulfion Oxidation with CO_2 Reduction over Highly Dispersed p-Bi Nanosheets and CO_2-Assisted Sulfur Extraction, Angew. Chem. Int. Ed. (2023) e202318585.

[28] F. Ye, S. Zhang, Q. Cheng, Y. Long, D. Liu, R. Paul, Y. Fang, Y. Su, L. Qu, L. Dai, C. Hu, The role of oxygen-vacancy in bifunctional indium oxyhydroxide catalysts for electrochemical coupling of biomass valorization with CO_2 conversion, Nat. Commun. 14 (2023) 2040.

[29] D.-D. Ma, S.-G. Han, C. Cao, W. Wei, X. Li, B. Chen, X.-T. Wu, Q.-L. Zhu, Bifunctional single-molecular heterojunction enables completely selective CO_2-to-CO conversion integrated with oxidative 3D nano-polymerization, Energy Environ. Sci. 14 (2021) 1544–1552.

[30] J. Wang, X. Li, M. Wang, T. Zhang, X. Chai, J. Lu, T. Wang, Y. Zhao, D. Ma, Electrocatalytic Valorization of Poly(ethylene terephthalate) Plastic and CO_2 for Simultaneous Production of Formic Acid, ACS Catal. 12 (2022) 6722–6728.

[31] Y. Li, N.M. Adli, W. Shan, M. Wang, M.J. Zachman, S. Hwang, H. Tabassum, S. Karakalos, Z. Feng, G. Wang, C. Li, G. Wu, Atomically Dispersed Single Ni Site Catalysts for High-Efficiency CO_2 Electroreduction at Industrial-Level Current Densities, Energy Environ. Sci. 15 (2022) 2108–2119.

[32] J.Y. Zhang, H. Wang, Y. Tian, Y. Yan, Q. Xue, T. He, H. Liu, C. Wang, Y. Chen, B. Y. Xia, Anodic Hydrazine Oxidation Assists Energy-Efficient Hydrogen Evolution over a Bifunctional Cobalt Perselenide Nanosheet Electrode, Angew. Chem. Int. Ed. 57 (2018) 7649–7653.

[33] L.-S. Wu, X.-P. Wen, H. Wen, H.-B. Dai, P. Wang, Palladium decorated porous nickel having enhanced electrocatalytic performance for hydrazine oxidation, J. Power Sources 412 (2019) 71–77.

[34] Q. Qian, J. Zhang, J. Li, Y. Li, X. Jin, Y. Zhu, Y. Liu, Z. Li, A. El-Harairy, C. Xiao, G. Zhang, Y. Xie, Artificial heterointerfaces achieve delicate reaction kinetics towards hydrogen evolution and hydrazine oxidation catalysis, Angew. Chem. Int. Ed. 60 (2021) 5984–5993.

[35] Y. Liu, J. Zhang, Y. Li, Q. Qian, Z. Li, Y. Zhu, G. Zhang, Manipulating dehydrogenation kinetics through dual-doping Co_3N electrode enables highly

[36] efficient hydrazine oxidation assisting self-powered H_2 production, Nat. Commun. 11 (2020) 1853.

[36] Q. Zhu, C.J. Murphy, L.R. Baker, Opportunities for Electrocatalytic CO_2 Reduction Enabled by Surface Ligands, J. Am. Chem. Soc. 144 (2022) 2829–2840.

[37] X. Ren, J. Zhao, X. Li, J. Shao, B. Pan, A. Salame, E. Boutin, T. Groizard, S. Wang, J. Ding, X. Zhang, W.Y. Huang, W.J. Zeng, C. Liu, Y. Li, S.F. Hung, Y. Huang, M. Robert, B. Liu, In-situ spectroscopic probe of the intrinsic structure feature of single-atom center in electrochemical CO/CO_2 reduction to methanol, Nat. Commun. 14 (2023) 3401.

[38] D. Xi, J. Li, J. Low, K. Mao, R. Long, J. Li, Z. Dai, T. Shao, Y. Zhong, Y. Li, Z. Li, X. J. Loh, L. Song, E. Ye, Y. Xiong, Limiting the Uncoordinated N Species in M-N_x Single-Atom Catalysts toward Electrocatalytic CO_2 Reduction in Broad Voltage Range, Adv. Mater. 34 (2022) e2104090.

[39] X. Wang, S. Feng, W. Lu, Y. Zhao, S. Zheng, W. Zheng, X. Sang, L. Zheng, Y. Xie, Z. Li, B. Yang, L. Lei, S. Wang, Y. Hou, A New Strategy for Accelerating Dynamic Proton Transfer of Electrochemical CO_2 Reduction at High Current Densities, Adv. Funct. Mater. 31 (2021) 2104243.

[40] H. Yang, Q. Lin, C. Zhang, X. Yu, Z. Cheng, G. Li, Q. Hu, X. Ren, Q. Zhang, J. Liu, C. He, Carbon dioxide electroreduction on single-atom nickel decorated carbon membranes with industry compatible current densities, Nat. Commun. 11 (2020) 593.

[41] H.B. Yang, S.-F. Hung, S. Liu, K. Yuan, S. Miao, L. Zhang, X. Huang, H.-Y. Wang, W. Cai, R. Chen, J. Gao, X. Yang, W. Chen, Y. Huang, H.M. Chen, C.M. Li, T. Zhang, B. Liu, Atomically dispersed Ni(i) as the active site for electrochemical CO_2 reduction, Nat. Energy 3 (2018) 140–147.

[42] H. Zhang, W. Zhou, T. Chen, B.Y. Guan, Z. Li, X.W. Lou, A modular strategy for decorating isolated cobalt atoms into multichannel carbon matrix for electrocatalytic oxygen reduction, Energy Environ. Sci. 11 (2018) 1980–1984.

[43] Y. Xue, Y. Li, G. Luo, K. Shi, E. Liu, J. Zhou, Using a Dynamic Inhibition Concept to Achieve Content-Controllable Synthesis of N-Coordinated Cu Atoms as Reversible Active Site toward Super Li-Ion Capacitors, Adv. Energy Mater. 10 (2020) 2002644.

[44] X. Wang, X. Sang, C.L. Dong, S. Yao, L. Shuai, J. Lu, B. Yang, Z. Li, L. Lei, M. Qiu, L. Dai, Y. Hou, Proton capture strategy for enhancing electrochemical CO_2 reduction on atomically dispersed metal-nitrogen active sites, Angew. Chem. Int. Ed. 60 (2021) 11959–11965.

[45] C. Hu, Y. Zhang, A. Hu, Y. Wang, X. Wei, K. Shen, L. Chen, Y. Li, Near- and long-range electronic modulation of single metal sites to boost CO_2 electrocatalytic reduction, Adv. Mater. 35 (2023) 2209298.

[46] W. Shan, R. Liu, H. Zhao, Z. He, Y. Lai, S. Li, G. He, J. Liu, Situ Surface-Enhanced Raman Spectroscopic Evidence on the Origin of Selectivity in CO_2 Electrocatalytic Reduction, ACS Nano 14 (2020) 11363–11372.

[47] P. Wang, S. Meng, B. Zhang, M. He, P. Li, C. Yang, G. Li, Z. Li, Sub-1 nm Cu_2O Nanosheets for the Electrochemical CO_2 Reduction and Valence State-Activity Relationship, J. Am. Chem. Soc. 145 (2023) 26133–26143.

[48] Q. Wang, K. Liu, J. Fu, C. Cai, H. Li, Y. Long, S. Chen, B. Liu, H. Li, W. Li, X. Qiu, N. Zhang, J. Hu, H. Pan, M. Liu, Atomically Dispersed s-Block Magnesium Sites for Electroreduction of CO_2 to CO, Angew. Chem. Int. Ed. 60 (2021) 25241–25245.

[49] L. Zhang, J. Feng, L. Wu, X. Ma, X. Song, S. Jia, X. Tan, X. Jin, Q. Zhu, X. Kang, J. Ma, Q. Qian, L. Zheng, X. Sun, B. Han, Oxophilicity-Controlled CO_2 Electroreduction to C_{2+} Alcohols over Lewis Acid Metal-Doped $Cu^{\delta+}$ Catalysts, J. Am. Chem. Soc. 145 (2023) 21945–21954.

[50] L. Zhang, D. Liu, S. Hao, L. Xie, F. Qu, G. Du, A.M. Asiri, X. Sun, Electrochemical hydrazine oxidation catalyzed by iron phosphide nanosheets array toward energy-efficient electrolytic hydrogen production from water, ChemistrySelect 2 (2017) 3401–3407.

[51] Z. Chen, N. Han, R. Zheng, Z. Ren, W. Wei, B.J. Ni, Design of earth-abundant amorphous transition metal-based catalysts for electrooxidation of small molecules: Advances and perspectives, SusMat 3 (2023) 290–319.

[52] Z. Zhang, P. Tang, H. Wen, P. Wang, Bicontinuous nanoporous Ni-Fe alloy as a highly active catalyst for hydrazine electrooxidation, J. Alloy. Compd. 906 (2022) 164370.

[53] W. Lai, Y. Qiao, J. Zhang, Z. Lin, H. Huang, Design strategies for markedly enhancing energy efficiency in the electrocatalytic CO_2 reduction reaction, Energy Environ. Sci. 15 (2022) 3603–3629.